JACS
JOURNAL OF THE AMERICAN CHEMICAL SOCIETY
Article
pubs.acs.org/JACS

# Electrochemically Active Nitrogen-Enriched Nanocarbons with Well-Defined Morphology Synthesized by Pyrolysis of Self-Assembled Block Copolymer

Mingjiang Zhong,[‡,†] Eun Kyung Kim,[△,†,‡] John P. McGann,[†] Sang-Eun Chun,[§] Jay F. Whitacre,[§,∥] Mietek Jaroniec,[#] Krzysztof Matyjaszewski,[†] and Tomasz Kowalewski*[,†]

[†]Department of Chemistry, Carnegie Mellon University, 4400 Fifth Avenue, Pittsburgh, Pennsylvania 15213, United States

[§]Department of Material Science and Engineering, Carnegie Mellon University, 5000 Forbes Avenue, Pittsburgh, Pennsylvania 15213, United States

[∥]Department of Engineering and Public Policy, Carnegie Mellon University, 5000 Forbes Avenue, Pittsburgh, Pennsylvania 15213, United States

[#]Department of Chemistry, Kent State University, Kent, Ohio 44242, United States

Supporting Information

**ABSTRACT:** Novel nanoporous nitrogen-enriched carbon materials were prepared through a simple carbonization procedure of well-defined block copolymer precursors containing the source of carbon, i.e., polyacrylonitrile (PAN), and a sacrificial block, i.e., poly(*n*-butyl acrylate) (PBA). The preparation of nitrogen-enriched nanocarbons with hierarchical pore structure was enabled by the high fidelity preservation of the initial phase-separated nanostructure between two polymer blocks upon carbonization. Supercapacitors fabricated from the prepared carbons exhibited unusually high capacitance per unit surface area (>30 $\mu$F/cm$^2$) which was attributed to the pseudocapacitance resulting from the high nitrogen content originating from the PAN precursor. Electrochemical availability of the nitrogen species was also evident from the results of oxygen reduction experiments. The hierarchical pore structure and the high nitrogen content in such materials make them particularly promising for use in supercapacitor and electrocatalyst applications.

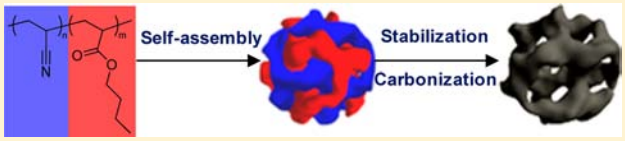


## INTRODUCTION

Over the past few decades, significant effort has been devoted to the development of new nanostructured materials with novel physical, chemical, and biological properties.[1] Carbon materials have occupied a special place in these developments due to the discovery and synthesis of new nanostructured carbon allotropes, such as fullerenes, nanotubes, and more recently graphene.[2] Another widely studied class of nanostructured carbons includes nanoporous carbons, which have a wide utility in a number of applications including filters, catalysts, and energy storage/conversion devices such as hydrogen reservoirs for fuel cells and supercapacitor or lithium-ion battery electrodes.[3]

In conjunction with the emergence of these new forms of nanostructured carbons there has been a resurgence of interest in the introduction of heteroatoms into carbon frameworks, primarily with the goal of introducing new functionalities to modify properties. The introduction of nitrogen has been particularly widely pursued in this regard,[4] with motivation ranging from modification of electronic properties,[5] artificial photosynthesis in water splitting[6] and $CO_2$ activation,[7] achieving electrocatalytic activity for oxygen reduction reaction (ORR),[3c,8] $CO_2$ capture,[9] or improvement of electrode performance in supercapacitors.[10] In the latter two instances, it is clear that such purposefully introduced heteroatoms need to be highly accessible to the "outside world", i.e. they need to be well presented on the external or internal (for porous systems) accessible surface of the material.

Herein we demonstrate a convenient generic synthetic pathway for preparation of such nitrogen-enriched nanoporous carbons which assures simultaneous control of nanoporosity and electrochemical accessibility of the nitrogen heteroatoms. This approach is predominately based on our earlier work on the design of carbon nanostructures through the use of well-defined block copolymers containing polyacrylonitrile (PAN) as a precursor for nitrogen-enriched carbon and a sacrificial block, i.e., poly(*n*-butyl acrylate) (PBA), serving as a source of mesoporosity.[11] Two promising aspects of such copolymer-templated nitrogen-enriched porous carbons (CTNC) include the potential to tune the morphology and porosity by varying the lengths and ratios of PAN and PBA blocks, and the straightforward mechanism for the incorporation of nitrogen atoms into a carbon framework. At first glance, copolymer templating appears to have a major (and potentially fatal) weakness, given concerns that the nanostructure resulting from

**Received:** May 4, 2012
**Published:** August 15, 2012



dx.doi.org/10.1021/ja304352n | J. Am. Chem. Soc. 2012, 134, 14846−14857

**Scheme 1. Preparation of CTNC**

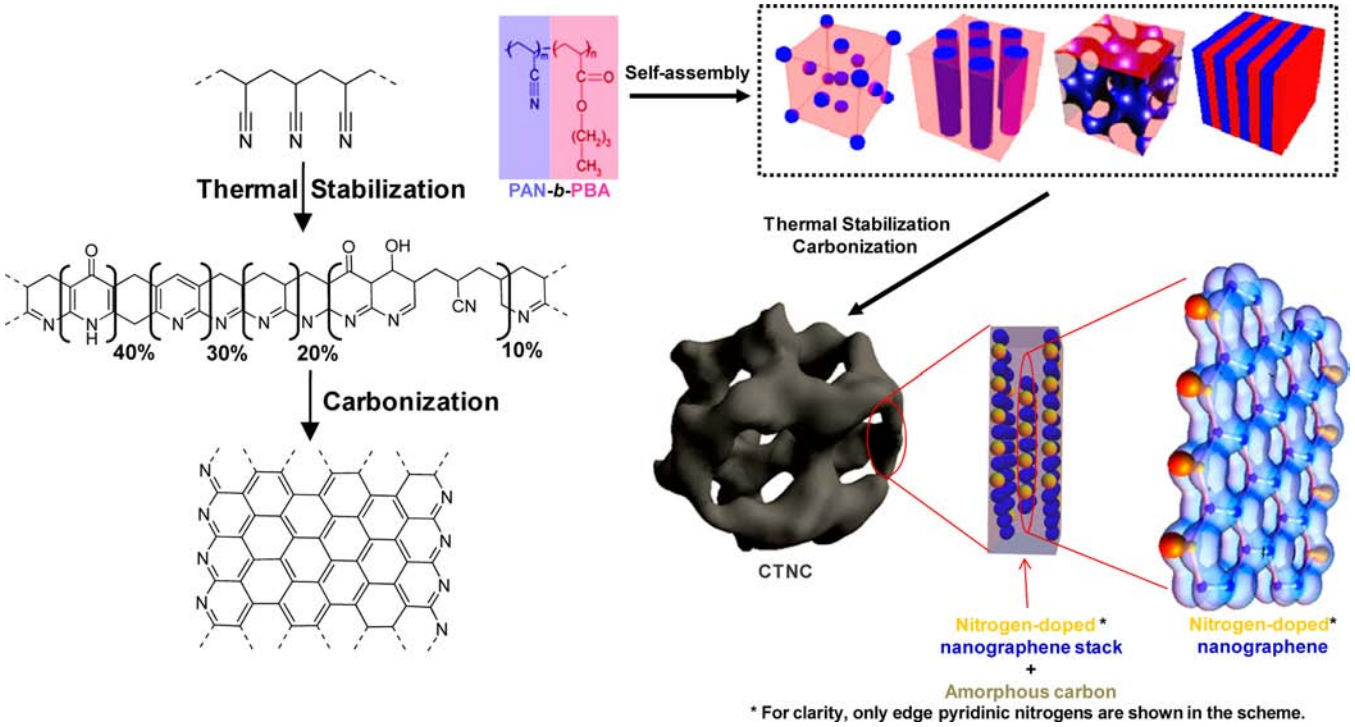


phase separation between the blocks may not survive after high temperature treatment necessary for carbonization. However, we previously demonstrated that this difficulty may be overcome through the use of a thermal stabilization step,[11a] comprising heating the copolymer in the presence of air, which effectively fixes the nanostructure through cross-linking reactions accompanied by partial dehydrogenation and cyclization of PAN (Scheme 1, and Scheme S1 in Supporting Information).[12] The retention of a high level of fidelity in the preservation of the nanostructure upon conversion from copolymer to carbon was particularly evident in ultrathin films with long-range ordered lamellar structures,[11b,13] although one should keep in mind that templating fidelity could have been facilitated by the presence of film substrate, preventing collapse of the nanostructure. Applicability of copolymer templating to bulk materials would require similar preservation of the nanostructure in the bulk, under conditions when the starting material is a block copolymer in a highly dispersed powder form. While this appears more challenging, we demonstrate below that it can be accomplished through the choice of the copolymer with PAN content high enough to lead to the formation of a continuous carbon framework, not susceptible to collapse upon pyrolysis.

After the high fidelity of nanostructure templating was established, the next focus of the research was the nitrogen doping aspect, establishing the chemical identity of nitrogen atoms incorporated into the carbon framework, and demonstrating their electrochemical availability, which is shown to enhance the performance of supercapacitors with electrodes fabricated from CTNCs. Additional evidence of electrochemical activity of nitrogen dopants comes from experiments in which CTNCs exhibit capability to electrochemically catalyze ORR.

## EXPERIMENTAL SECTION

**Materials.** Acrylonitrile (AN), *n*-butyl acrylate (BA), methyl 2-bromopropionate (MBP), *N*,*N*,*N*′,*N*″,*N*″-pentamethyldiethylenetriamine (PMDETA), 2,2′-bipyridyl (bpy), CuBr, CuCl, $CuBr_2$, anisole, dimethylformamide (DMF), dimethyl sulfoxide (DMSO), tetrahydrofuran (THF), *N*-methyl-2-pyrrolidone (NMP), ethanol, methanol, and Nafion117 solution (5 wt %) were all obtained from Sigma-Aldrich. CuCl and CuBr were purified by stirring in glacial acetic acid followed by washing with ether and dried overnight under vacuum. Monomers were passed through a basic alumina column prior to use. All other chemicals were used as received.

**Preparation of PBA Macroinitiator.** Thirty milliliters of BA ($2.10 \times 10^{-1}$ mol), $2.24 \times 10^{-1}$ mL of PMDETA ($1.07 \times 10^{-3}$ mol), $1.99 \times 10^{-1}$ mL of MBP ($1.79 \times 10^{-3}$ mol), 2.0 mg of $CuBr_2$ ($9 \times 10^{-3}$ mmol), and 15 mL of anisole were mixed in a 50 mL Schlenk flask equipped with a magnetic stirring bar. The flask was subjected to five freeze−pump−thaw (FPT) cycles. Then, $1.28 \times 10^{-1}$ g of CuBr ($8.93 \times 10^{-4}$ mol) was added to the flask while the contents were at a solid state and deoxygenated by vacuum followed by backfilling with nitrogen three times. The flask was placed in an oil bath set at 70 °C for 5.5 h. The reaction was terminated by the addition of aerated THF and passing through a column of alumina to remove the catalyst followed by evaporation. The solid products were dried in a vacuum oven.

**Preparation of PBA-*b*-PAN Copolymers.** A 1.11 g amount of the above PBA macroinitiator ($1.23 \times 10^{-4}$ mol; $M_n$ (GPC) = 9000 and $M_w/M_n$ = 1.10), 2.57 mL of AN ($3.96 \times 10^{-2}$ mol), and 4.0 mL of DMSO were mixed in a 10 mL Schlenk flask equipped with a magnetic stirring bar. The flask was subjected to five FPT cycles. Then, $1.22 \times 10^{-2}$ g of CuCl ($1.23 \times 10^{-4}$ mol) and $3.85 \times 10^{-2}$ g of bpy ($2.46 \times 10^{-4}$ mol) were added to the flask, as above, and purged by backfilling with nitrogen. The flask was then placed in an oil bath set at 65 °C for 7 h. At the end of this time, the reaction mixture was dissolved in DMF, and the polymer was precipitated by adding the solution to 50% aqueous methanol. The solid product was dried under vacuum.

**Preparation of CTNC.** The polymer sample was stabilized at 280 °C for 2 h under air flow (150 mL/min) with a heating rate of 20 °C/min, purged with nitrogen gas for 1 h during cooling, and then pyrolyzed at 700 °C for 0.5 h under nitrogen gas flow (150 mL/min) with a heating rate of 10 °C/min.

**$CO_2$ Activation of CTNC.** The nanoporous carbon sample was heated at a rate of 20 °C/min under nitrogen gas flow (150 mL/min)


dx.doi.org/10.1021/ja304352n | J. Am. Chem. Soc. 2012, 134, 14846−14857

to 900 °C and kept at that temperature under $CO_2$ flow (150 mL/min) for 1 h. Then, the sample was cooled under nitrogen gas flow.

**KOH Activation of CTNC.** Deionized water was added to the mixture of KOH and carbon at a mass ratio of 4/1 and stirred for 30 min. The slurry was dried at 110 °C for 12 h, heated to 800 °C with a rate of 5 °C/min, and maintained at that temperature for 2 h under Ar flow. The resultant activated carbon was rinsed with 0.5 M HCl and repeatedly washed with hot deionized water. The final activated carbon was dried under vacuum at 90 °C for 2 days.

**Characterization of CTNC.** The mass change during the carbonization was monitored by thermogravimetric analysis (TGA: SDT 2960, TA Instruments). The nanoporous morphology of CNTC was analyzed by transmission electron microscopy (TEM: H-7100, Hitachi). Nitrogen adsorption−desorption isotherms were obtained with a NOVA 2000 (Quantachrome Instruments) at −196 °C. The sample was degassed at 300 °C for 2 h before measurement. Elemental analysis was conducted by Midwest Microlab (Indianapolis, IN) with a combustion method analyzer (CE-440, Exter Analytical Inc.) and with X-ray photoelectron spectroscopy (XPS, Kratos Axis Ultra spectrometer). Small angle X-ray scattering (SAXS) experiments was carried out at D1 station of Cornell High Energy Synchrotron Source (CHESS). A wide bandpass (1.7%) double-bounce multilayer monochromator supplied an intense beam of 10 keV photons. The SAXS scattering intensities were recorded with an area detector (Medoptics) with a resolution of 50 $\mu$m per pixel and a total area of about 50 mm by 50 mm. The scattering data was collected at a distance of 1888 mm and 562 mm from the sample to the detector.

**Fabrication of Supercapacitor Devices.** After carbonization, the nanoporous carbon was ground with a mortar and pestle. Electrodes were prepared by drop-casting a 50 mg/mL carbon dispersion in NMP onto a stainless steel mesh (400 mesh, Small Parts Inc.) with a diameter of 13 mm. Before the casting, the dispersion was stirred for ∼20 min and sonicated ∼10 min. The solid in the dispersion consisted of 85 wt % of CTNC, 5 wt % of acetylene black as a conductive additive, and 10 wt % of poly(vinylidene fluoride) as a binder. The drop-casted samples were dried on a 70 °C hot stage for 2 h and further dried in a 100 °C vacuum oven overnight. The mass of the dried electrodes was in the range of 2−4 mg. Two-electrode cells using Teflon Swagelok were built and tested. Paper filters were used as separators.

**Electrochemical Characterization.** The electrochemical properties were determined using a multichannel potentiostat/galvanostat (VMP, Biologic) in 1 M aqueous $H_2SO_4$ and 6 M aqueous KOH electrolyte. The cyclic voltammetry (CV) curves were obtained at various scan rates from 1 to 100 mV/s in the range of 0 to 1 V. Galvanostatic charge−discharge (CD) curves were obtained at various current densities from 0.1 A/g to 10 A/g. The mass-normalized capacitance of a single electrode ($C_g$) was calculated from the galvanostatic discharging curve according to, $1/C = 1/C_A + 1/C_B = 1/(C_g m_A) + 1/(C_g m_B) = 1/C_g(1/m_A + 1/m_B)$, thus

$$C_g = \frac{I}{\Delta V(t)/\Delta t}\left(\frac{1}{m_A} + \frac{1}{m_B}\right) \quad (1)$$

where $m_A$ and $m_B$ are the active carbon masses of the two electrodes, and $I$, $\Delta V(t)$, and $\Delta t$ are the loading current, full discharging voltage window (1 V) including all IR drop regions, and discharging time, respectively. The current density was defined as $I \times (1/m_A + 1/m_B)$. Electrochemical impedance spectroscopy (EIS) measurements were performed in the frequency range of $10^5$ Hz to $10^{-3}$ Hz at the open circuit potential with an AC perturbation of 5 mV.

**ORR Characterization.** A glassy carbon (GC) electrode (3 mm, from Gamry) was carefully polished with 3 $\mu$m, 1 $\mu$m, and 0.25 $\mu$m diamond successively to obtain a mirror-like surface. Then the electrode was washed with double-distilled water and acetone and finally dried in air. One milligram of carbon was dissolved in 1 mL of solvent mixture of Nafion (5%) and ethanol (v/v = 1/9) by sonication. Twenty microliters of the solution was dropcasted on the GC electrode surface and dried in air. All of the voltammograms were recorded at 25 °C with a Gamry Reference 600 potentiostat. Measurements were carried out at a scan rate of 10 mV/s or 100 mV/s using the as-prepared GC working electrode and a platinum disk counter electrode in $N_2$-saturated or $O_2$-saturated 0.1 M KOH aqueous solution. Potentials were recorded versus a saturated calomel electrode (SCE) reference electrode.

## RESULTS AND DISCUSSION

**Fidelity of Nanostructure Templating in CTNC.** Preparation of CNTCs from phase-separated block copolymers containing a carbon source (PAN) and sacrificial block (PBA) is illustrated in Scheme 1. The copolymers were synthesized using methods assuring a high level of control over the block length and composition in order to maintain control of nanoscale morphology arising from phase separation between the blocks. In the current study this was achieved through the use of atom transfer radical polymerization (ATRP).[14] Several block copolymers with different block ratios were prepared and tested, but herein we focus on the system with the nanoscale phase-separated morphology which provided the best preservation of nanostructure after pyrolysis: PBA-*b*-PAN diblock copolymer with the average composition $(BA)_{70}$-$(AN)_{99}$ and molecular weight distribution $M_w/M_n = 1.25$, where $M_w$ and $M_n$ are, respectively, the weight and number average molecular weights. The as-obtained polymer in the form of a precipitated powder was heated at 20 °C/min to 280 °C, held at that temperature for 2 h under air flow, undergoing a process of stabilization, prior to pyrolysis at 700 °C for 30 min under flow of nitrogen gas.

The weight loss associated with this thermal treatment was studied by TGA (Figure 1), which revealed the presence of

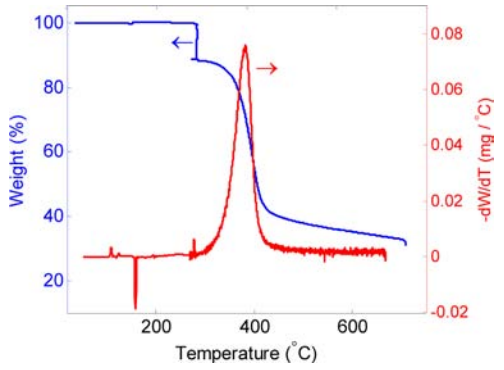


**Figure 1.** TGA and differential thermogravimetry (DTG) showing weight changes during thermal stabilization and pyrolysis of PAN-*b*-PBA copolymer. The thermal stabilization step involved heating the copolymer in air at 20 °C/min to 280 °C and holding at this temperature and atmosphere for 2 h (vertical drop in weight). Weight loss at temperatures above 280 °C occurred during the pyrolysis step which involved heating the stabilized sample at 10 °C/min under nitrogen flow to 700 °C and holding it there for 0.5 h.

three distinct stages: (1) stabilization of PAN, which was accompanied by ∼10% weight loss due to partial dehydrogenation and cross-linking; (2) decomposition of PBA with a total weight loss of ∼50% between 350 and 410 °C; (3) carbonization of PAN with further dehydrogenation and partial denitrogenation.

The XRD pattern of such prepared CTNC revealed the presence of broad Bragg peaks indicative of the presence of nanographitic structures commonly observed in pyrolytic carbons (Figure 2).[15] A crude estimate of the lateral size of partially graphitic domains based on the width of the (100)


dx.doi.org/10.1021/ja304352n | J. Am. Chem. Soc. 2012, 134, 14846−14857

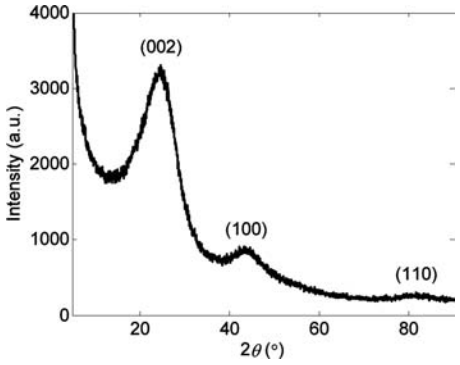


**Figure 2.** XRD profiles of CTNC: The (002) diffraction peak centered at a $2\theta \sim 25°$ corresponds to $\pi$-stacking of nanographitic platelets, and the width of the (100) peak centered at a $2\theta \sim 44°$ can be used to assess their lateral size $L_a$.

peak indicated that they did not exceed 2−3 nm. Likewise, based on the width of the (002) peak, nanographitic domains were composed of no more than two to three $\pi$-stacked nanographene sheets.

The evolution of the nanoscale phase-separated morphology from PBA-*b*-PAN block copolymer precursor to carbon was characterized by transmission SAXS and is presented in Figure 3a and 3b, in the form of overlaid double logarithmic plots of azimuthally averaged, invariant normalized scattering patterns. In Figure 3a the scattering patterns were shifted vertically for clarity. The scattering pattern of the as-precipitated block

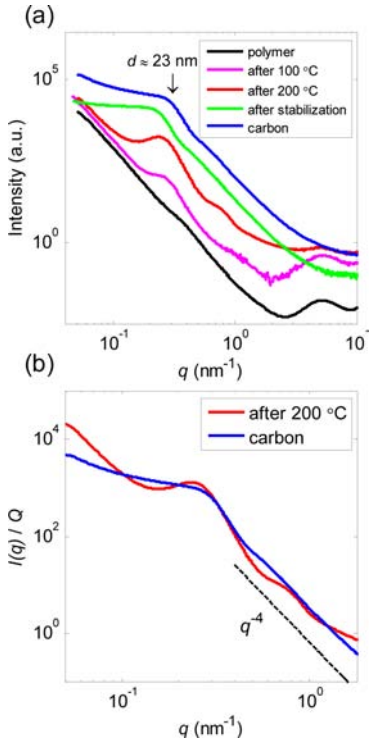


**Figure 3.** SAXS characterization of nanoscale morphology. (a) SAXS profiles of block copolymer and resulting carbon after subsequent thermal treatment stages. The curves have been shifted vertically for clarity. (b) Overlay of SAXS profiles of block copolymer with nanoscale morphology fully developed by annealing and of resulting nanocarbon. The profiles shown here were normalized by the Porod invariant Q and overlaid without any vertical shifting.

copolymer powder, black line in Figure 3a, showed uniform $q^{-4}$ decay for $q$ extending up to $\sim 2$ nm$^{-1}$, most likely indicating the presence of scale-invariant, self-similar aggregates of precipitated powder. It was devoid of other distinct features, pointing to the absence of well-defined nanoscale morphology. Local ordering due to phase separation became evident only after annealing at 100 °C through the appearance of a broad Bragg peak at 0.27 nm$^{-1}$ (spacing ~23 nm), which became more pronounced upon further annealing at 200 °C (magenta and red traces Figure 3a). After stabilization, the position of the Bragg peak shifted downward by about 0.05 nm$^{-1}$ to lower $q$ after stabilization (green trace in Figure 3a) only to return to its previous position after carbonization (blue trace in Figure 3a and Figure 3b). All these observations provide a strong indication that the overall nanoscale morphology of block copolymer template was retained after decomposition of the sacrificial block and carbonization of PAN. A modest shift of the Bragg position between stabilized and carbonized sample is not unexpected and can be explained as a consequence of a combination of nonisotropic contraction/expansion of the PAN framework upon cross-linking followed by isotropic contraction upon carbonization. One other interesting feature of the double logarithmic plot of the scattering pattern observed both for the stabilized and carbonized material is the pronounced decrease of the slope in the low-$q$ range in comparison with the copolymer precursor, down to ~−2 for carbonized sample in comparison with ~−4 for a copolymer. This behavior indicates that upon carbonization, aggregates of polymer particles present in the powder underwent fusion to generate more monolithic structures. Of critical importance here is the fact that despite this fusion, the nanoscale porosity of material was fully retained, as evident from the overall preservation of position and intensity of the Bragg peak and from more detailed analysis of SAXS patterns presented below.

The uniform, nonfractal, nanoporous structure of CTNC was also evident in TEM images (Figure 4). The characteristic length of the features observed in the TEM images, inferred from the kink in the power spectrum of the 2-D Fourier transform (inset in Figure 4), was in good agreement with the

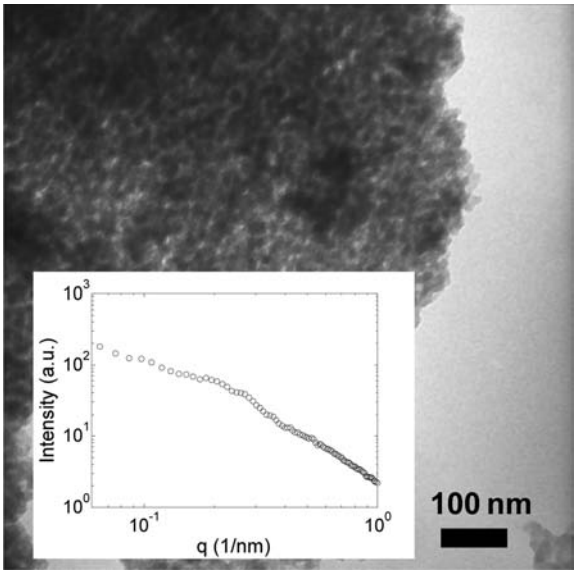


**Figure 4.** TEM image of CTNC. Inset: power spectrum of the Fourier transform of the image.


dx.doi.org/10.1021/ja304352n | J. Am. Chem. Soc. 2012, 134, 14846−14857

position of the Bragg peak observed in SAXS patterns. Moreover, just as with the SAXS pattern, the low-$q$ region in the double logarithmic plot of the TEM power spectrum was nearly flat, reflecting the absence of complex aggregation on the scale from ∼10 to 1000 nm.

The most common use of SAXS in the studies of block copolymers and other nanomaterials involves identification of types of three-dimensional morphologies based on the position and intensities of Bragg peaks arising from long-range periodicities. In fact, the high degree of perfection of the long-range order in templated nanomaterials is widely sought and equated with the high quality of the material. Importantly, its presence greatly simplifies the task of assessing the fidelity of templating, which can be inferred from the extent to which the SAXS patterns change upon material transformations. From this perspective, our system might appear rather unremarkable, given the fact that its SAXS patterns reveal only the first order, diffuse Bragg feature. At this point it should be emphasized, however, that while long-range order may be highly aesthetically appealing, the key figure of merit in nanoporous materials is their specific surface area, typically ascertained through adsorption isotherm measurements. In copolymer templating of the kind employed here, with porosity originating from the removal of the sacrificial phase, the specific surface area should somehow correspond to the specific interfacial area between copolymer phases. One well-established SAXS technique capable of directly characterizing the specific interfacial area in isotropic two-phase materials is so-called Porod analysis, which is based on the analysis of the characteristic decay rate of normalized scattering patterns.[16] With proper normalization, application of this analysis to selected length scale yields the specific interfacial area originating from the density fluctuations within a given length range. Thus, seemingly uninteresting SAXS patterns can still be a rich source of information about the key figures of merit for high-surface systems. According to this well-known law, for an isotropic two-phase material with a sharp interface between the phases, the normalized scattering intensity varies as

$$\frac{I(q)}{Q} = \frac{8\pi}{l_P}\frac{1}{q^4} \qquad (2)$$

where $Q$ is a normalized factor referred to as an invariant and $l_P$ denotes the length of inhomogeneity, defined as the geometric average of cord lengths cut through phases **1** and **2**: $1/\langle l_P\rangle = 1/\langle l_1\rangle + 1/\langle l_2\rangle$, where indices refer to phases **1** and **2** and $\langle\ \rangle$ brackets indicate orientational and positional averaging (see Supporting Information for details). As evident in Figure 3b, the high-$q$ portions of invariant-normalized scattering patterns of a copolymer template and carbon nearly overlap and closely follow the $q^{-4}$ scaling, with minor deviations for a copolymer caused by the presence of a weak higher order Bragg peak and high-$q$ electron density fluctuations. The calculations of $l_P$ were carried out from fits to eq 2 as described in Supporting Information, over the scattering vector range $q_{min}$ = 0.4 nm$^{-1}$ (i.e., just above the Bragg peak) and $q_{max}$ = 1.8 nm$^{-1}$. The upper limit, which corresponds to ∼3.5 nm in real space, was chosen to minimize the contribution from high-$q$ electron density fluctuations. Such obtained lengths of inhomogeneity for a copolymer template and carbon were equal to $l_{P,template}$ = 7.4 nm and $l_{P,carbon}$ = 7.6 nm, respectively, providing further evidence for the preservation of template morphology upon carbonization.

Of particular usefulness in the analysis of porous materials is the relationship between the length of inhomogeneity and the interfacial area to volume ratio $S_V = (4\phi_1\phi_2)/l_P$, where $\phi_1$, $\phi_2$ are volume fractions of phases **1** and **2** ($\phi_1 + \phi_2 = 1$). The copolymer template volume fractions of PAN and PBA were calculated by taking the mass fractions, known from well-defined copolymer composition obtained from nuclear magnetic resonance (NMR) spectra, and converting them to volume fractions, assuming that the densities of PBA and PAN phases were equal to the densities of respective homopolymers and yielding ultimately the interfacial area to volume ratio $S_{V,template}$ = 123 m$^2$/cm$^3$ (see Supporting Information for details). Volume fractions of carbon matrix and pores necessary for the analogous calculation for the porous carbon were obtained using the total pore volume per gram ($V_{tot}$) calculated from nitrogen adsorption analysis and the density of the carbon matrix. It is remarkable that the value obtained for the interfacial area to volume ratio $S_{V,carbon}$ = 131 m$^2$/cm$^3$ was close to the value obtained for the copolymer template, providing further indication of the high fidelity retention of the nanostructure throughout the templating process.

Direct information about the porosity of CTNC was obtained through standard nitrogen adsorption analysis using the Kruk–Jaroniec–Sayari (KJS) method (see Supporting Information for details).[17] The nitrogen adsorption–desorption isotherm recorded for CTNC and the corresponding pore size distribution (PSD) curve, which was calculated from the adsorption branch of the isotherm, are shown in Figure 5. The

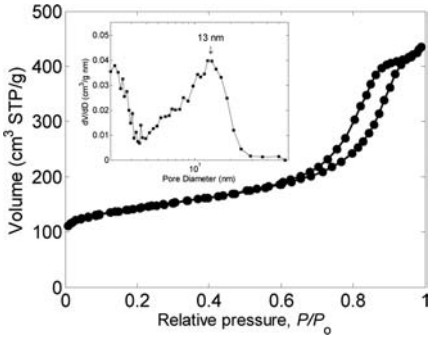


**Figure 5.** Nitrogen sorption isotherm at −196 °C of CTNC and the corresponding pore size distribution (inset) calculated from the adsorption branch of the isotherm using the KJS method.

nitrogen adsorption isotherm recorded for CTNC is type IV, based on IUPAC 1985 classification, because it exhibits a distinct hysteresis loop at relative pressures of 0.6–0.9, H1 type according to IUPAC classification. This can be ascribed to the filling and emptying of the mesopores by capillary condensation/evaporation, respectively.[18] The PSD curve indicates the presence of mesopores and has a maximum at the pore diameter of ∼13 nm.

The Brunauer–Emmett–Teller (BET) specific surface area ($S_{BET}$) of the CTNC sample was estimated to be ∼500 m$^2$/g. Its total pore volume ($V_{tot}$) was calculated as 0.67 cm$^3$/g based on the amount adsorbed at a relative pressure of 0.99. The micropore surface area obtained using the $\alpha_s$-plot method (Figure S1 in Supporting Information) was found to be $S_{mic}$ = 240 m$^2$/g while the KJS method yielded a total mesopore surface area of $S_{mes}$ = 236 m$^2$/g. When attempting to compare the mesopore surface area with the surface to volume ratio obtained from Porod analysis of SAXS patterns, one must keep


dx.doi.org/10.1021/ja304352n | J. Am. Chem. Soc. 2012, 134, 14846–14857

in mind that the latter was restricted to the real space size range down to 3.5 nm. Integration of the pore size distribution obtained from nitrogen adsorption analysis using the same lower limit gives a value of 180 $m^2/g$, which after conversion to the surface per volume ratio, $S_V$ (see Supporting Information), translates to 147 $m^2/cm^3$. The latter value is in good agreement with the interface to volume ratio obtained from SAXS analysis ($S_{V,carbon}$ = 131 $m^2/cm^3$), providing further evidence that the mesopores were the direct result of copolymer templating. Moreover, such agreement provides a strong indication of good accessibility for all mesopores. In addition to templated mesopores, in similarity with other templated porous carbons, CTNC contained a considerable amount of micropores, which are usually traced to structural imperfections of the carbon precursor and partial local destruction of the evolving carbonizing matrix.

These results demonstrate remarkable resistance of phase-separated $(BA)_{70}$-$(AN)_{99}$ copolymer against structural collapse during pyrolysis to form the carbon framework and can serve as a proof of concept for a one-step, single-component templating of porous carbons using block copolymers with carefully chosen composition.

**Identifying Nitrogen Atoms Incorporated into the Carbon Framework.** Elemental analysis (combustion method), shown in Table 1, revealed a high nitrogen content in CTNC pyrolyzed at 700 °C, with N/C atomic ratio equal to 0.18, indicating that at least 50% of nitrogen atoms originally present in the PAN precursor remained incorporated within the carbon framework. The fine structure of the N 1s peak in XPS (Figure 6a) points to the presence of three major species of nitrogen differentiated by their binding energies (BE): (i) pyridinic (N−P, BE ≈ 398.5 eV), (ii) mixture of pyridonic (N−X, BE ≈ 400.6 eV) and pyrrolic (BE ≈ 400.3 eV), and (iii) pyridine oxide (N−O, BE ≈ 403−405 eV).[19] The chemical environments of these nitrogen atoms revealed by XPS, 35% pyridinic, 43% pyridonic + pyrrolic, and 20% pyridine oxide, appear to be consistent with their location along the outer edges of nanographitic domains, which would explain their electrochemical availability, as described later. It is also worth noting that the full width at the half-maximum (fwhm) of the N−P peak observed here was almost one-half of the width reported in literature for the pyridinic nitrogen in pyrolytic carbons derived from PAN, ∼1.3 eV vs ∼2 eV,[19] pointing to the unusual degree of uniformity in the chemical environment of this species in our material. Such uniformity can be interpreted as another indication of preferential location of pyridinic nitrogen atoms in CTNC on the exposed surfaces of pore walls, i.e., in the environment where they do not come into close contact with other neighbors. It should be pointed out that of all nitrogen species, the pyridinic ones, with the lone pair residing on the $sp^2$ orbital which is not a part of the aromatic system, can be expected to be most electrochemically active.[20] A relatively low fraction (2%) of quaternary nitrogen species (N−Q, BE = 401.4 eV) was also observed. On the basis of the carbonization mechanism of PAN, this fraction can be ascribed to graphitic nitrogens in CTNC.

**Structural and Chemical Changes of CNTC Caused by Activation Treatment.** Pyrolytic carbons are commonly subjected to an "activation" treatment, which typically involves high temperatures, between 700 °C and 1000 °C, and exposure of the material to $CO_2$, steam, or KOH and results in a significant increase of surface area, primarily due to the formation of micropores.[10b,21] In order to study the impact of this kind of a treatment on the nanostructure and chemical composition of nitrogen-enriched carbons with well-defined nanostructure such as CTNC described in the present study, material previously carbonized for 30 min at 700 °C was subjected to $CO_2$ activation and KOH activation.

**Table 1. Physicochemical Properties and Specific Capacitance Values of CTNC, $CO_2$-Activated CTNC (CO2-A), and KOH-Activated CTNC (KOH-A)**

| | CTNC | CO2-A | KOH-A |
|---|---|---|---|
| surface area, $S_{BET}$ ($m^2/g$) | 500 | 1140 | 2570 |
| Chemical Composition[a] | | | |
| elemental analysis | | | |
| H/C (%) | 20.1 | 7.4 | 9.9 |
| O/C (%) | 3.6 | 4.7 | 5.7 |
| N/C (%) | 18.0 | 4.8 | 0.9 |
| XPS | | | |
| O/C (%) | 7.3 ± 0.4 | 5.4 ± 0.4 | 8.3 ± 0.4 |
| N/C (%) | 13.5 ± 0.8 | 4.1 ± 0.5 | 1.4 ± 0.5 |
| N−P | | | |
| BE (eV) | 398.5 | 398.5 | |
| N−P/C (%) | 4.8 | 0.5 | |
| fwhm | 1.3 | 1.0 | |
| N−X | | | |
| BE (eV) | 400.6 | 400.6 | 400.6 |
| N−X/C (%) | 5.8 | 1.9 | 1.0 |
| fwhm | 2.2 | 3.8 | 2.6 |
| N−Q | | | |
| BE (eV) | 401.3 | 401.4 | |
| N−Q/C (%) | 0.2 | 0.7 | |
| fwhm | 1.3 | 1.1 | |
| N−O | | | |
| BE (eV) | 403.5 | 403.5 | 404.6 |
| N−O/C (%) | 2.7 | 1.1 | 0.4 |
| fwhm | 6.2 | 5.8 | 5.1 |
| Crystallinity | | | |
| $L_a$ (nm) | 1.9 ± 0.3 | 4.3 ± 0.5 | 2.8 ± 0.2 |
| Capacitance | | | |
| 1 M $H_2SO_4$ | | | |
| $C_g$ (F/g) | 166 ± 5 | 164 ± 4 | 176 ± 9 |
| $C_{sa}$ ($\mu F/cm^2$) | 33.2 | 14.3 | 6.8 |
| 6 M KOH | | | |
| $C_g$ (F/g) | 124 ± 3 | 151 ± 9 | 173 ± 7 |
| $C_{sa}$ ($\mu F/cm^2$) | 24.8 | 13.2 | 6.7 |

[a]Percent of atomic ratio.

As is commonly observed in other pyrolytic carbons, activation in all cases led to marked increase of the specific surface area of CTNC. Figure 7 shows nitrogen adsorption−desorption isotherms and the corresponding PSDs of CTNC, $CO_2$-activated CTNC (CO2-A), and KOH-activated CTNC (KOH-A). The impact of processing conditions on the other physicochemical properties of materials is summarized in Table 1 and Table S1. Both activation methods resulted in significant increases of the specific surface area, more than 2-fold to $S_{BET}$ = 1140 $m^2/g$ for CO2-A and 5-fold to $S_{BET}$ = 2570 $m^2/g$, for KOH-A. A comparison of PSDs of activated materials with untreated CTNC, Figure 7b, indicates that $CO_2$ activation left the fraction of mesopores previously attributed to copolymer


dx.doi.org/10.1021/ja304352n | J. Am. Chem. Soc. 2012, 134, 14846−14857

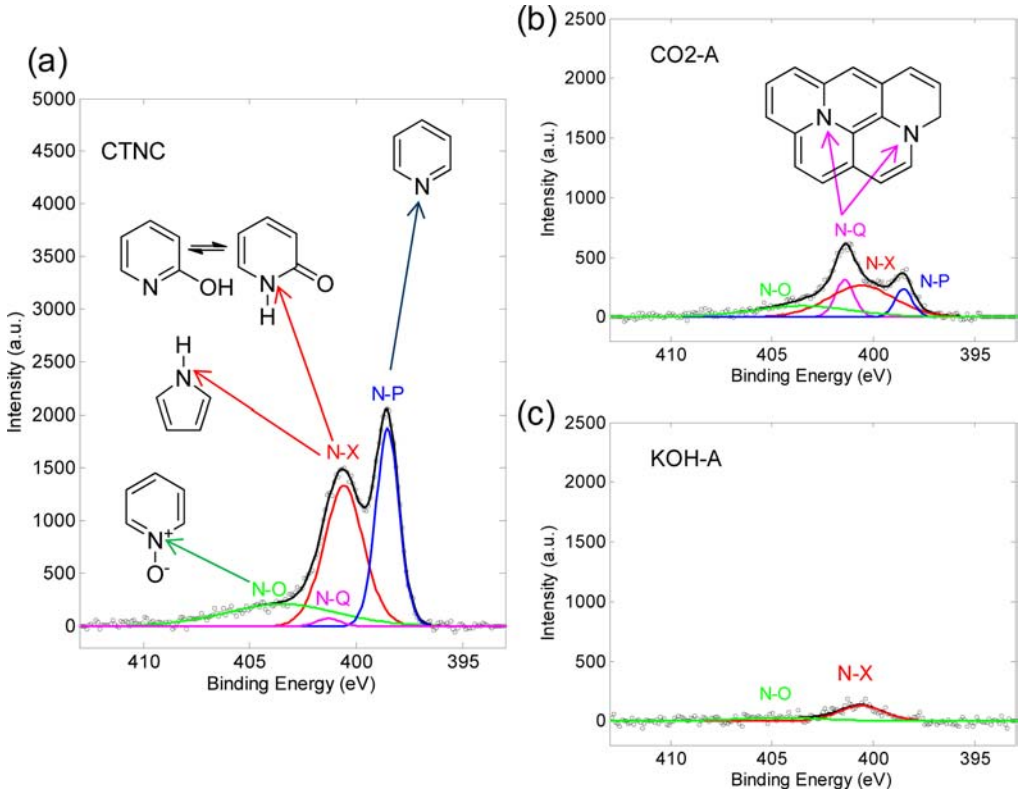


**Figure 6.** N 1s peaks in XPS of pristine and activated CTNCs: (a) pristine CTNC; (b) $CO_2$-activated CTNC (CO2-A); (c) KOH-activated CTNC (KOH-A).

templating almost intact. For KOH activation, however, the shape of PSD changed dramatically, with small pores, about 3 nm in dimension, becoming the dominant feature.

Preservation of the mesoporous structure in $CO_2$-activated material and its collapse upon KOH activation was also evident in the SAXS patterns (Figure S2 in Supporting Information). In addition, KOH activation also had a very pronounced effect on wide angle XRD patterns, Figure 8, causing the (002), $\pi$-stacking peak to broaden beyond recognition. At the same time, the basal (100) peak remained relatively unchanged, indicating that KOH virtually exfoliated the nanographitic $\pi$-stacks. A similar mechanism for KOH activation has been described by other authors for conventional activated carbons.[22] This decrease in $\pi$-stacking order with preservation of the basal peak was also evident in the $CO_2$-activated system but was not nearly as prominent as with KOH activation. Additionally, analysis of basal plane crystallite sizes ($L_a$) calculated from the width of (100) peak XRD patterns using the Scherrer equation[23] provided evidence of ring fusion of nanographitic domains during the activation treatment. Specifically, the value of $L_a$ changed from 1.9 nm in the pristine CTNC to 4.3 nm after $CO_2$ activation and to 2.8 nm after KOH treatment, Table 1. The more pronounced increase of $L_a$ after $CO_2$ activation can be attributed to the higher temperature used in this process in comparison with KOH activation, 900 °C vs 800 °C.

The most noticeable chemical effect of activation was the sharp drop in nitrogen content: 4-fold for $CO_2$ activation and ~20-fold for KOH process, Table 1. This drop could be partially attributed to a temperature treatment higher than that used for normal pyrolysis conditions, i.e., 900 °C for $CO_2$ activation and 800 °C for KOH activation vs 700 °C for normal pyrolysis. Activation also had a pronounced and partially selective effect on the chemical nature of the remaining nitrogen species. For example, following $CO_2$ activation, the pyridinic nitrogen atoms (N−P) exhibited a 10-fold decrease while the concentration of pyridonic + pyrrolic (N−X) and pyridine oxide (N−O) groups only decreased by a factor of 3, Table 1 and Figure 6a,b. Another marked effect of $CO_2$ activation was the emergence of quaternary nitrogen peak (N−Q) as a dominant feature (Figure 6b). The latter effect appears to indicate that one of the side effects of $CO_2$ activation was fusion of nanographitic domains in which edge nitrogen atoms became entrapped within a carbon lattice, in agreement with the currently accepted mechanism of PAN pyrolysis, Figure S3 in Supporting Information,[19] and the increased basal plane crystallite size ($L_a$) after activation in XRD, Figure 8. Remarkably, no pyridinic or quartenary nitrogen atoms were discernible in the XPS spectra of KOH-activated material, Figure 6c and Table 1, which showed only trace amounts of N−X and N−O species. Such behavior points to a highly destructive effect from KOH treatment on the carbon framework, which, as discussed above, was also evident in XRD patterns, Figure 8.

**CTNC and Activated CTNCs as Electrode Materials for Supercapacitors.** One of the purposes of experiments with CTNCs as electrode materials for supercapacitors was to establish if their high nitrogen content offers any electrochemical advantage, such as giving rise to Faradaic processes (pseudocapacitance),[10] which could enhance the energy storage capabilities.

In supercapacitors, porous carbons serve as high surface area electrodes, capable of storing energy in electrical double layers (EDLs) when placed in contact with an electrolyte. The high surface area of porous electrodes boosts the overall stored


dx.doi.org/10.1021/ja304352n | J. Am. Chem. Soc. 2012, 134, 14846−14857

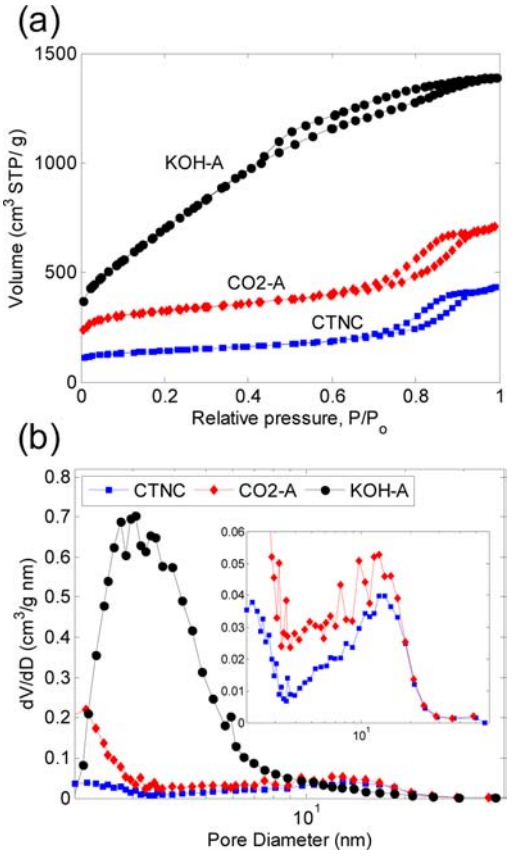


**Figure 7.** Pore characterization results for activated CTNCs: (a) nitrogen sorption isotherms at −196 °C for the CTNC, $CO_2$-activated CTNC (CO2-A), and KOH-activated CTNC (KOH-A) samples and (b) the corresponding PSDs calculated by the KJS method using adsorption branches of the isotherms (inset: a magnified figure showing only PSDs for the CTNC and CO2-A samples).

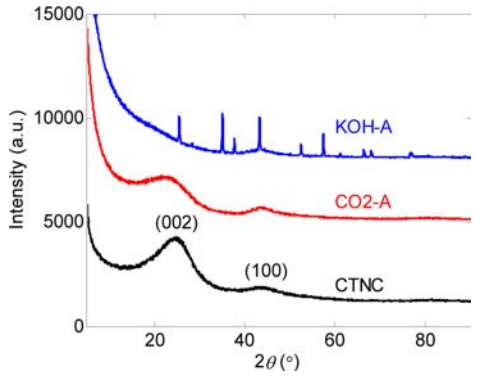


**Figure 8.** XRD profiles of CTNC, $CO_2$-activated CTNC (CO2-A), and KOH-activated CTNC (KOH-A). The curves were shifted vertically for a clear comparison.

energy density, while the EDL charge storage mechanism assures a high power density. Supercapacitors are particularly promising in such applications as hybrid electric vehicles, digital communication devices, and backup energy storage.[24] However, the energy storage density of supercapacitors is still inferior in comparison with batteries. A common approach to overcoming this limitation is through the introduction of an additional charge storage mechanism, i.e. pseudocapacitance, involving fast and reversible redox reactions. One of the widely used ways to accomplish this is through the incorporation of electrochemically active phases such as metal oxides and conducting polymers.[25] Another particularly promising approach, related to work described herein, involves covalent incorporation of heteroatoms such as nitrogen or oxygen within the carbon framework.[10b,c,26]

To date, most of the applications and studies using carbons for supercapacitors have focused on activated carbons, which can be easily produced from a wide range of natural precursors and, following activation, can exhibit surface areas in excess of 2000 $m^2/g$.[10a] While the performance of supercapacitors is most directly affected by the total surface area, the pore structure and the shape of PSD are other key features that need to be optimized. The presence of mesopores, 2−50 nm in diameter, is desirable because they can ensure efficient propagation of ions throughout the bulk of the electrode material, whereas micropores, less than 2 nm in diameter, have an optimum pore size for the formation of EDLs.[10a,c,27] To some extent, this limits the suitability of activated carbons as supercapacitor electrode materials, because conventional activation methods do not ensure the desirable control of pore structure and PSD. This limitation has sparked research into new nanoporous carbon materials as electrodes, including carbon aerogels,[28] carbide-derived carbons,[3b,29] carbon nanotubes (CNTs),[30] graphenes,[1d,3d,31] and templated ordered mesoporous carbons (OMCs) from silica templates.[32]

Performance of CTNC materials synthesized in this study as supercapacitor electrodes was evaluated by employing two-electrode devices fabricated using common procedures, as described in Supporting Information. One molar aqueous $H_2SO_4$ and 6 M aqueous KOH were tested as electrolytes. Major electrochemical measurements included cyclic voltammetry (CV), Figure 9a, galvanostatic charge/discharge (CD), Figure 9b, and electrochemical impedance spectroscopy (EIS), Figure 9d. The CV curves (Figure 9a) and CD (Figure 9b) curves in 1 M $H_2SO_4$ have nearly rectangular and triangular shapes, respectively, indicating that the behavior approaches that of an ideal capacitor. Even at a high scan rate of 100 mV/s, the CV curve maintained this shape with only a slight loss of capacitance, implying fast electrolyte movement within the electrodes. The specific capacitance ($C_g$) was found to be 166 F/g at 0.1 A/g and retained 77% of this value (127 F/g) at a high loading current density of 10 A/g of, Figure 9c. This rate capability indicates that the interconnected micro/mesopore structure provides an efficient pathway for electrolyte ion movement through the carbon matrix.[33] Importantly, studied devices exhibited good cyclability, which is especially desirable in supercapacitors, by maintaining 85% of capacitance after 14000 charge/discharge cycles at 2 A/g, Figure 10. In addition, the EIS results pointed to a relatively low contribution from the resistive component to the device impedance, with the equivalent series and parallel resistances equal to 0.2 Ω and 0.8 Ω, respectively, Figure 9d. These low resistance values can explain the good rate capabilities of the cell. Accordingly, $C_g$ measured at low frequency ($10^{-3}$ Hz) calculated from the EIS data using equation, $C = -1/(2\pi f Z'')$ where $f$ is the frequency, was very close to the value obtained from the CD curve at 0.1 A/g (164 F/g vs 166 F/g). Also, the low-frequency segment of the EIS spectrum was nearly vertical, indicative of pure capacitor behavior unimpeded by resistance.

Altogether, the observed values of capacitance are within the range of capacitances typically reported for carbon-based supercapacitors (50−200 F/g).[34] What is of particular interest, however, is that they were achieved with an overall surface area

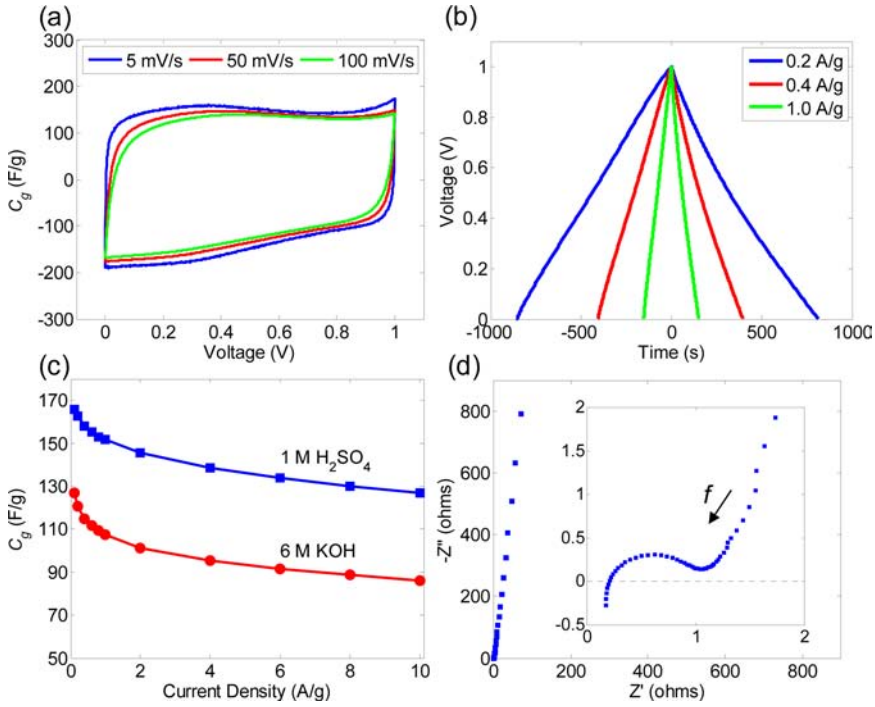


**Figure 9.** Characterization of supercapacitors built with CTNC electrodes: (a) cyclic voltammetry curves; (b) galvanostatic charge−discharge curves; (c) relationship between $C_g$ and current density; (d) Nyquist plot using a sinusoidal signal of 5 mV over the frequency range from $10^5$ Hz to $10^{-3}$ Hz at open circuit potential. The equivalent series resistance (ESR) corresponds to the *x*-intercept and a parallel resistance value is the diameter of the semicircle in the high frequency region. Plots a, b, and d show results obtained by using 1 M $H_2SO_4$ as an electrolyte. Mass of the electrodes: 2.8/3.0 mg for 1 M $H_2SO_4$, and 3.1/3.3 mg for 6 M KOH.

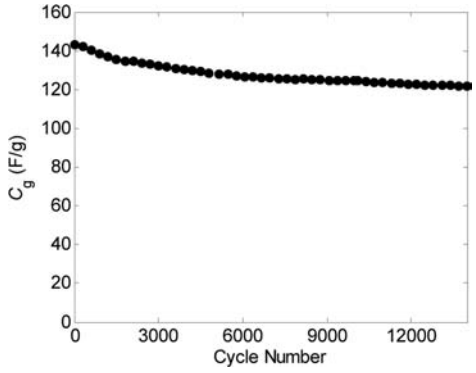


**Figure 10.** The cycling performance of the supercapacitor cell fabricated from CTNC at 2 A/g with 1 M $H_2SO_4$ electrolyte.

at least twice as low as the typical surface area of carbon-based electrodes (~500 $m^2/g$ vs 1000−2000 $m^2/g$). This difference is best captured by comparing the surface area-normalized capacitances, $C_{sa}$: ~33 $\mu F/cm^2$ for CTNC vs less than 10 $\mu F/cm^2$ for commercial activated carbons.[35] Such unusually high value of surface area-normalized capacitance in CTNC appears to confirm our expectation that the abundance of nitrogen heteroatoms should be a source of pseudocapacitance. This assertion is further supported upon the closer inspection of the shape of CV curves of CTNC acquired at different scan rates in 1 M $H_2SO_4$ and 6 M KOH and their comparison with the respective curves acquired for devices with electrodes composed of a commercial activated carbon (YP-50F, Kuraray Chemical Co.), Figure S4a,b and S4c,d, respectively, Supporting Information. Specifically, CV curves recorded for CTNC in 1 M $H_2SO_4$ (Figure S4a) exhibited marked deviations from the nearly rectangular shape expected for an ideal EDL capacitor and observed for the activated carbon YP-50F. Interestingly, such deviations were not observed for CTNC in 6 M KOH electrolyte (Figure S4b). One of the possible explanations of such dependence of pseudocapacitive behavior on the type of electrolyte could be that it involves protonation/deprotonation of nitrogen atoms exposing the electron lone pair to solution, e.g., pyridinic species.[10a] It should be pointed out that in nitrogen-enriched materials, the pseudocapacitance originating from nitrogen is commonly ascribed to the ill-defined, broad redox features manifested as deviations of CV curves from the ideal rectangular shape.[10b,c,25b]

The most compelling evidence of the critical importance of nitrogen heteroatoms for supercapacitor performance came from the observation that even though both activation methods more than doubled the surface area of CTNC, they had only minor effect on mass-normalized capacitances (Table 1). As a result, the capacitance per unit surface area ($C_{sa}$) of CTNC exhibited a 2-fold to 5-fold decrease from its unusually high value of 33 $\mu F/cm^2$, thereby falling into the range commonly observed for activated carbons.

Analysis of the shapes of CV curves of $CO_2$- and KOH-activated CTC acquired with 1 M $H_2SO_4$ and 6 M KOH electrolyte (Figure S4e−h in Supporting Information) shows behavior consistent with loss of pseudocapacitance resulting from the loss of nitrogen atoms. It was particularly clear with KOH-activated material, for which the shape of CV curves now became much closer to rectangular, Figure S4g and S4h, indicating nearly ideal EDL behavior. Deviations from rectangular shape were still evident in $CO_2$-activated material, especially in 1 M $H_2SO_4$ electrolyte, Figure S4e, which is not surprising given the fact that after this activation method, the material still had appreciable nitrogen content (Table 1 and Figure 6b).


dx.doi.org/10.1021/ja304352n | J. Am. Chem. Soc. 2012, 134, 14846−14857

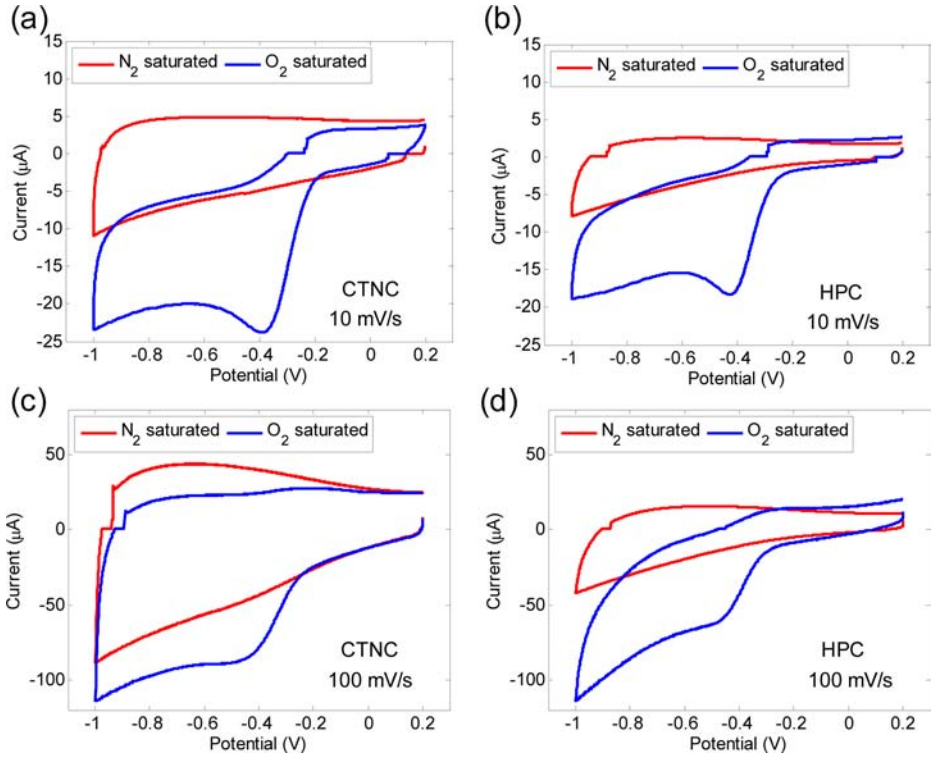


**Figure 11.** CV curves of CTNC and HPC on glassy carbon electrode for ORR (SCE as reference electrode) in $N_2$-saturated and $O_2$-saturated 0.1 M KOH aqueous solution: (a) CTNC at a scan rate of 10 mV/s; (b) HPC at a scan rate of 10 mV/s; (c) CTNC at a scan rate of 100 mV/s; (d) HPC at a scan rate of 100 mV/s.

**CTNC as Electrocatalyst for ORR.** In addition to their use as high surface area electrodes for energy storage devices, porous carbon materials are frequently used as supports for metal catalysts, for example in fuel cell technology, where they can support catalysts for oxidation of a fuel and reduction of oxygen. One of the very interesting and promising developments in this area is the series of findings that nitrogen-doped carbons including carbon nanotubes,[36] graphene,[8c] and their small-molecule analogues[37] can act as electrocatalysts for ORR even in the absence of any purposefully introduced metal centers.

The abundance and the electrochemical availability of the nitrogen species in CTNC described here suggests that our material could also serve as an ORR electrocatalyst. In order to explore this possibility, CV experiments with CTNC deposited on glassy carbon electrodes as described in the Experimental Section were conducted in both $N_2$-saturated (control) and $O_2$-saturated aqueous solutions of 0.1 M KOH, Figure 11a and 11c. While CV curves acquired in control experiments did not show any evidence of redox events, in the presence of bubbled $O_2$ they revealed the presence of a prominent reduction peak at the potential of −0.390 V, similar to the results reported in other ORR work with nitrogen-enriched carbons. To assess the role of high surface area of CTNC, additional control experiments were performed with carbon prepared by pyrolysis of homopolymer PAN (HPC) carried out under the same conditions, Figure 11b and 11d. As expected, the CV curve for this material also had a pronounced feature at −0.426 V, which could be ascribed to ORR. Interestingly, while the ORR peak in CTNC material appeared to be more pronounced (Figure 11a and 11b) and better defined at higher scan rate (Figure 11c and 11d), the difference was not as dramatic as one might expect, given the large difference in surface areas between CTNC and HPC, i.e., 500 $m^2/g$ vs 70 $m^2/g$. This indicates that for the scan rates used here, the ORR occurred primarily at the outer surface of the electrode and did not appear to benefit from the mesoporosity present in the CTNC, probably due to kinetic reasons.

## CONCLUSIONS AND OUTLOOK

Block copolymers containing a nitrogen-rich source of carbon, i.e., PAN, and a sacrificial block, i.e., PBA, can be converted into nitrogen-enriched porous carbons (one nitrogen atom per five to six carbon atoms) with the final carbon nanostructure faithfully "molded" by the nanostructure of a block copolymer and containing hierarchically arranged micro- and mesopores. Combined SAXS and nitrogen adsorption analysis revealed that the size and total surface area of interconnected mesopores formed upon removal of the sacrificial block, here ~180 $m^2/g$, was in a very good agreement with the domain size and interfacial area of the block copolymer template. Micropores, dispersed throughout the bulk of the carbon framework, provided additional 240 $m^2/g$ surface area in the CTNC material. It is worth noticing that while the Bragg features in SAXS patterns of block copolymers and CTNCs were rather ill-defined, pointing to the poorly defined long-range periodicity, Porod analysis of SAXS patterns revealed the presence of sharp interface and high interfacial area, which was very well preserved after pyrolysis.

The combination of high surface area and good electrochemical accessibility of nitrogen atoms originating from the PAN precursor, manifested by remarkably high capacitance per unit surface area and by the electrocatalysis of ORR, indicates the considerable promise of CTNCs as materials for energy storage and catalysis. The simplicity and scalability of the described synthetic method and the potential for significant


dx.doi.org/10.1021/ja304352n | J. Am. Chem. Soc. 2012, 134, 14846−14857

enhancement of already good performance of CTNCs through straightforward means, such as the increase of fraction of pyridinic nitrogen sites (e.g., through the use of milder stabilization conditions) or the increase of surface area (e.g., by decreasing the length of PAN and PBA blocks), further add to this promise. One considerable challenge associated with the proposed lower molecular weight systems may be in striking the balance between order−disorder transition and thermal stabilization.

## ■ ASSOCIATED CONTENT

### Supporting Information

Details of experimental methods, a scheme of the PAN carbonization mechanism, $\alpha_s$-plot of CTNC, and SAXS profiles of the activated CTNC. This material is available free of charge via the Internet at http://pubs.acs.org.

## ■ AUTHOR INFORMATION


### Corresponding Author

tomek@andrew.cmu.edu

### Present Address

△Battery R&D, AMD PJT, LG Chem Research Park, LG Chem, 104-1, Moonji-dong, Yuseong-gu, Daejeon, 305-738, Korea.

### Author Contributions

‡These authors contributed equally to this work.


### Notes

The authors declare no competing financial interest.

## ■ ACKNOWLEDGMENTS

Financial support was provided by the National Science Foundation (DMR-0304508 and DMR 09-69301), the Air Force Office of Scientific Research, and Carnegie Mellon University. A portion of this work was carried out at the Cornell High Energy Synchrotron Source (CHESS), Cornell University, which is partially supported by the National Science Foundation (DMR-0936384).

## ■ REFERENCES


(1) (a) Moriarty, P. *Rep. Prog. Phys.* **2001**, *64*, 297−381. (b) Wang, Z. L.; Song, J. *Science* **2006**, *312*, 242−246. (c) Cayrol, B.; Nogues, C.; Dawid, A.; Sagi, I.; Silberzan, P.; Isambert, H. *J. Am. Chem. Soc.* **2009**, *131*, 17270−17276. (d) Deng, Y.; Cai, Y.; Sun, Z.; Liu, J.; Liu, C.; Wei, J.; Li, W.; Liu, C.; Wang, Y.; Zhao, D. *J. Am. Chem. Soc.* **2010**, *132*, 8466−8473. (e) Endo, M.; Katsuda, Y.; Hidaka, K.; Sugiyama, H. *J. Am. Chem. Soc.* **2010**, *132*, 1592−1597. (f) Morin, S. A.; Bierman, M. J.; Tong, J.; Jin, S. *Science* **2010**, *328*, 476−480. (g) Tisdale, W. A.; Williams, K. J.; Timp, B. A.; Norris, D. J.; Aydil, E. S.; Zhu, X.-Y. *Science* **2010**, *328*, 1543−1547.

(2) Pierson, H. O. *Handbook of carbon, graphite, diamond, and fullerenes: properties, processing, and applications*; Noyes Publications: Park Ridge, NJ., 1993.

(3) (a) Lee, J.; Kim, J.; Hyeon, T. *Adv. Mater.* **2006**, *18*, 2073−2094. (b) Simon, P.; Gogotsi, Y. *Nat. Mater.* **2008**, *7*, 845−854. (c) Gong, K.; Du, F.; Xia, Z.; Durstock, M.; Dai, L. *Science* **2009**, *323*, 760−764. (d) Liu, C. G.; Yu, Z. N.; Neff, D.; Zhamu, A.; Jang, B. Z. *Nano Lett.* **2010**, *10*, 4863−4868. (e) Zhu, Y.; Murali, S.; Stoller, M. D.; Ganesh, K. J.; Cai, W.; Ferreira, P. J.; Pirkle, A.; Wallace, R. M.; Cychosz, K. A.; Thommes, M.; Su, D.; Stach, E. A.; Ruoff, R. S. *Science* **2011**, *332*, 1537−1541. (f) Guo, B. K.; Wang, X. Q.; Fulvio, P. F.; Chi, M. F.; Mahurin, S. M.; Sun, X. G.; Dai, S. *Adv. Mater.* **2011**, *23*, 4661−4666. (g) Wu, D.; Dong, H.; Pietrasik, J.; Kim, E. K.; Hui, C. M.; Zhong, M.; Jaroniec, M.; Kowalewski, T.; Matyjaszewski, K. *Chem. Mater.* **2011**, *23*, 2024−2026. (h) Wu, D.; Hui, C. M.; Dong, H.; Pietrasik, J.; Ryu, H. J.; Li, Z.; Zhong, M.; He, H.; Kim, E. K.; Jaroniec, M.; Kowalewski, T.; Matyjaszewski, K. *Macromolecules* **2011**, *44*, 5846−5849.

(4) (a) Vinu, A.; Ariga, K.; Mori, T.; Nakanishi, T.; Hishita, S.; Golberg, D.; Bando, Y. *Adv. Mater.* **2005**, *17*, 1648−1652. (b) Groenewolt, M.; Antonietti, M. *Adv. Mater.* **2005**, *17*, 1789−1792. (c) McGann, J. P.; Zhong, M.; Kim, E. K.; Natesakhawat, S.; Jaroniec, M.; Whitacre, J. F.; Matyjaszewski, K.; Kowalewski, T. *Macromol. Chem. Phys.* **2012**, *213*, 1078−1090.

(5) (a) Wang, X.; Li, X.; Zhang, L.; Yoon, Y.; Weber, P. K.; Wang, H.; Guo, J.; Dai, H. *Science* **2009**, *324*, 768−771. (b) Yan, Q.; Huang, B.; Yu, J.; Zheng, F.; Zang, J.; Wu, J.; Gu, B.-L.; Liu, F.; Duan, W. *Nano Lett.* **2007**, *7*, 1469−1473.

(6) Wang, X.; Maeda, K.; Thomas, A.; Takanabe, K.; Xin, G.; Carlsson, J. M.; Domen, K.; Antonietti, M. *Nat. Mater.* **2009**, *8*, 76−80.

(7) Goettmann, F.; Thomas, A.; Antonietti, M. *Angew. Chem., Int. Ed.* **2007**, *46*, 2717−2720.

(8) (a) Jin, X.; Balasubramanian, V. V.; Selvan, S. T.; Sawant, D. P.; Chari, M. A.; Lu, G. Q.; Vinu, A. *Angew. Chem., Int. Ed.* **2009**, *48*, 7884−7887. (b) Tang, Y.; Allen, B. L.; Kauffman, D. R.; Star, A. *J. Am. Chem. Soc.* **2009**, *131*, 13200−13201. (c) Liu, Y.; Qu, L. T.; Baek, J. B.; Dai, L. M. *ACS Nano* **2010**, *4*, 1321−1326. (d) Yang, S. B.; Feng, X. L.; Wang, X. C.; Müllen, K. *Angew. Chem., Int. Ed.* **2011**, *50*, 5339−5343.

(9) (a) Hao, G.-P.; Li, W.-C.; Qian, D.; Lu, A.-H. *Adv. Mater.* **2010**, *22*, 853−857. (b) Li, Q.; Yang, J.; Feng, D.; Wu, Z.; Wu, Q.; Park, S.; Ha, C.-S.; Zhao, D. *Nano Res.* **2010**, *3*, 632−642.

(10) (a) Frackowiak, E. *Phys. Chem. Chem. Phys.* **2007**, *9*, 1774−1785. (b) Ra, E. J.; Raymundo-Pinero, E.; Lee, Y. H.; Beguin, F. *Carbon* **2009**, *47*, 2984−2992. (c) Yang, X.; Wu, D.; Chen, X.; Fu, R. *J. Phys. Chem. C* **2010**, *114*, 8581−8586.

(11) (a) Kowalewski, T.; Tsarevsky, N. V.; Matyjaszewski, K. *J. Am. Chem. Soc.* **2002**, *124*, 10632−10633. (b) Tang, C. B.; Tracz, A.; Kruk, M.; Zhang, R.; Smilgies, D. M.; Matyjaszewski, K.; Kowalewski, T. *J. Am. Chem. Soc.* **2005**, *127*, 6918−6919.

(12) Fitzer, E. *Carbon* **1989**, *27*, 621−645.

(13) Tang, C.; Wu, W.; Smilgies, D.-M.; Matyjaszewski, K.; Kowalewski, T. *J. Am. Chem. Soc.* **2011**, *133*, 11802−11809.

(14) (a) Tang, C. B.; Kowalewski, T.; Matyjaszewski, K. *Macromolecules* **2003**, *36*, 1465−1473. (b) Tang, C. B.; Qi, K.; Wooley, K. L.; Matyjaszewski, K.; Kowalewski, T. *Angew. Chem., Int. Ed.* **2004**, *43*, 2783−2787. (c) Tang, C.; Dufour, B.; Kowalewski, T.; Matyjaszewski, K. *Macromolecules* **2007**, *40*, 6199−6205.

(15) Bonino, F.; Brutti, S.; Reale, P.; Scrosati, B.; Gherghel, L.; Wu, J.; Müllen, K. *Adv. Mater.* **2005**, *17*, 743−746.

(16) Roe, R. J. *Methods of X-ray and neutron scattering in polymer science*; Oxford University Press: New York, 2000.

(17) (a) Kruk, M.; Jaroniec, M.; Sayari, A. *Langmuir* **1997**, *13*, 6267−6273. (b) Choma, J.; Jaroniec, M.; Kloske, M. *Adsorpt. Sci. Technol.* **2002**, *20*, 307−315.

(18) Rouquerol, F.; Rouquerol, J.; Sing, K. S. W. *Adsorption by powders & porous solids: principles, methodology and applications*; Academic Press: San Diego, CA, 1999.

(19) Pels, J. R.; Kapteijn, F.; Moulijn, J. A.; Zhu, Q.; Thomas, K. M. *Carbon* **1995**, *33*, 1641−1653.

(20) (a) Yang, S. B.; Feng, X. L.; Wang, X. C.; Mullen, K. *Angew. Chem., Int. Ed.* **2011**, *50*, 5339−5343. (b) Liu, R.; Wu, D.; Feng, X.; Müllen, K. *Angew. Chem., Int. Ed.* **2010**, *49*, 2565−2569. (c) Yu, D.; Zhang, Q.; Dai, L. *J. Am. Chem. Soc.* **2010**, *132*, 15127−15129.

(21) Kierzek, K.; Frackowiak, E.; Lota, G.; Gryglewicz, G.; Machnikowski, J. *Electrochim. Acta* **2004**, *49*, 515−523.

(22) (a) Yamashita, Y.; Ouchi, K. *Carbon* **1982**, *20*, 41−45. (b) Lu, C. L.; Xu, S. P.; Gan, Y. X.; Liu, S. Q.; Liu, C. H. *Carbon* **2005**, *43*, 2295−2301.

(23) Kinoshita, K. *Carbon: electrochemical and physicochemical properties*; Wiley: New York, 1988.

(24) (a) Conway, B. E. *Electrochemical supercapacitors: scientific fundamentals and technological applications*; Plenum Press: New York, 1999. (b) Miller, J. R.; Simon, P. *Science* **2008**, *321*, 651−652.

(25) (a) Conway, B. E.; Pell, W. G. *J. Solid State Electrochem.* **2003**, *7*, 637−644. (b) Liang, Y.; Schwab, M. G.; Zhi, L.; Mugnaioli, E.; Kolb, U.; Feng, X.; Müllen, K. *J. Am. Chem. Soc.* **2010**, *132*, 15030−15037. (c) Patel, M. N.; Wang, X.; Slanac, D. A.; Ferrer, D. A.; Dai, S.; Johnston, K. P.; Stevenson, K. J. *J. Mater. Chem.* **2012**, *22*, 3160−3169. (d) Arbizzani, C.; Mastragostino, M.; Meneghello, L.; Paraventi, R. *Adv. Mater.* **1996**, *8*, 331−334.

(26) (a) Lota, G.; Grzyb, B.; Machnikowska, H.; Machnikowski, J.; Frackowiak, E. *Chem. Phys. Lett.* **2005**, *404*, 53−58. (b) Hulicova-Jurcakova, D.; Kodama, M.; Shiraishi, S.; Hatori, H.; Zhu, Z. H.; Lu, G. Q. *Adv. Funct. Mater.* **2009**, *19*, 1800−1809. (c) Frackowiak, E.; Lota, G.; Machnikowski, J.; Vix-Guterl, C.; Beguin, F. *Electrochim. Acta* **2006**, *51*, 2209−2214. (d) Beguin, F.; Szostak, K.; Lota, G.; Frackowiak, E. *Adv. Mater.* **2005**, *17*, 2380−2384. (e) Kim, C.; Ngoc, B. T. N.; Yang, K. S.; Kojima, M.; Kim, Y. A.; Kim, Y. J.; Endo, M.; Yang, S. C. *Adv. Mater.* **2007**, *19*, 2341−2346.

(27) Xu, F.; Cai, R.; Zeng, Q.; Zou, C.; Wu, D.; Li, F.; Lu, X.; Liang, Y.; Fu, R. *J. Mater. Chem.* **2011**, *21*, 1970−1976.

(28) (a) Wei, T. Y.; Chen, C. H.; Chien, H. C.; Lu, S. Y.; Hu, C. C. *Adv. Mater.* **2010**, *22*, 347−351. (b) Zeng, X.; Wu, D.; Fu, R.; Lai, H.; Fu, J. *Electrochim. Acta* **2008**, *53*, 5711−5715. (c) Wang, J.; Yang, X.; Wu, D.; Fu, R.; Dresselhaus, M. S.; Dresselhaus, G. *J. Power Sources* **2008**, *185*, 589−594. (d) Zeng, X.; Wu, D.; Fu, R.; Lai, H. *Mater. Chem. Phys.* **2008**, *112*, 1074−1077.

(29) Chmiola, J.; Yushin, G.; Gogotsi, Y.; Portet, C.; Simon, P.; Taberna, P. L. *Science* **2006**, *313*, 1760−1763.

(30) (a) Kaempgen, M.; Chan, C. K.; Ma, J.; Cui, Y.; Gruner, G. *Nano Lett.* **2009**, *9*, 1872−1876. (b) Izadi-Najafabadi, A.; Yasuda, S.; Kobashi, K.; Yamada, T.; Futaba, D. N.; Hatori, H.; Yumura, M.; Iijima, S.; Hata, K. *Adv. Mater.* **2010**, *22*, E235−E241.

(31) Miller, J. R.; Outlaw, R. A.; Holloway, B. C. *Science* **2010**, *329*, 1637−1639.

(32) (a) Joo, S. H.; Choi, S. J.; Oh, I.; Kwak, J.; Liu, Z.; Terasaki, O.; Ryoo, R. *Nature* **2001**, *412*, 169−172. (b) Ryoo, R.; Joo, S. H.; Kruk, M.; Jaroniec, M. *Adv. Mater.* **2001**, *13*, 677−681. (c) Wu, D.; Chen, X.; Lu, S.; Liang, Y.; Xu, F.; Fu, R. *Microporous Mesorporous Mater.* **2010**, *131*, 261−264.

(33) Liang, Y.; Wu, D.; Fu, R. *Langmuir* **2009**, *25*, 7783−7785.

(34) Liu, C.; Li, F.; Ma, L. P.; Cheng, H. M. *Adv. Mater.* **2010**, *22*, E28−E62.

(35) Zhang, L. L.; Zhao, X. S. *Chem. Soc. Rev.* **2009**, *38*, 2520−2531.

(36) (a) Dai, L. M.; Gong, K. P.; Du, F.; Xia, Z. H.; Durstock, M. *Science* **2009**, *323*, 760−764. (b) Star, A.; Tang, Y. F.; Allen, B. L.; Kauffman, D. R. *J. Am. Chem. Soc.* **2009**, *131*, 13200−13201.

(37) Baumgarten, M.; Liu, R. L.; von Malotki, C.; Arnold, L.; Koshino, N.; Higashimura, H.; Müllen, K. *J. Am. Chem. Soc.* **2011**, *133*, 10372−10375.